



Close Major-merger Pairs at $z = 0$: Bulge-to-total Ratio and Star Formation Enhancement

Chuan He^{1,2}, Cong Kevin Xu¹, Donovan Domingue³, Chen Cao^{4,5}, and Jia-sheng Huang¹¹ Chinese Academy of Sciences South America Center for Astronomy, National Astronomical Observatories of China, Chinese Academy of Sciences, Beijing 100101, People's Republic of China; congxu@nao.cas.cn² School of Astronomy and Space Sciences, University of Chinese Academy of Sciences, Beijing 100049, People's Republic of China³ Georgia College & State University, CBX 82, Milledgeville, GA 31061, USA⁴ School of Space Science and Physics, Shandong University, Weihai, Shandong 264209, People's Republic of China⁵ Shandong Key Laboratory of Optical Astronomy & Solar-Terrestrial Environment, Institute of Space Sciences, Shandong University, Weihai, Shandong 264209, People's Republic of China

Received 2021 December 13; revised 2022 May 20; accepted 2022 May 25; published 2022 July 29

Abstract

We present a study of the bulge-to-total ratio (B/T) of a K_s -band-selected sample of 88 close major-merger pairs of galaxies (H-KPAIR), based on two-dimensional decompositions of SDSS r -band images with GALFIT. We investigate the dependence of the interaction-induced specific star formation rate enhancement (sSFR_{enh}) on the B/T ratio, and the effects of this dependence on the differences between star-forming galaxies (SFGs) in spiral+spiral (S+S) and spiral+elliptical (S+E) pairs. Of all the 132 spiral galaxies in H-KPAIR, the 44 in S+E pairs show higher B/T than those in the 44 S+S pairs, with means of $B/T = 0.35 \pm 0.05$ and $B/T = 0.26 \pm 0.03$, respectively. There is a strong negative dependence of sSFR_{enh} on the B/T ratio, and only paired SFGs with $B/T < 0.3$ show significant ($>5\sigma$) enhancement. Paired SFGs in S+S pairs show a similar trend, and many disk SFGs ($B/T < 0.1$) in S+S pairs have strong sSFR enhancements (sSFR_{enh} > 0.7 dex). For SFGs in S+E pairs, the sSFR has no clear B/T dependence, nor any significant enhancement in any B/T bin. Disk SFGs in S+S pairs show significant ($>4\sigma$) enhancement in molecular gas content (M_{H_2}/M_{star}), while SFGs in S+E pairs have no such enhancement in any B/T bin. No significant enhancement of the total gas content (M_{gas}/M_{star}) is found in any B/T bin for paired galaxies. The star formation efficiency of either the total gas (SFE_{gas} = SFR/ M_{gas}) or molecular gas (SFE_{H₂} = SFR/ M_{H_2}) does not depend on the B/T ratio. The only significant ($>4\sigma$) SFE enhancement found for paired SFGs is the SFE_{gas} for disk SFGs in S+S pairs.

Unified Astronomy Thesaurus concepts: Galaxy evolution (594); Galaxy interactions (600); Galaxy structure (622); Star formation (1569)

1. Introduction

It has been well established that galaxy interactions and mergers can induce star formation enhancement (Toomre & Toomre 1972; Larson & Tinsley 1978; Kennicutt et al. 1987; Sanders & Mirabel 1996). In the local universe, the most extreme starbursts, such as ultraluminous infrared galaxies ($L_{IR} \geq 10^{12} L_{\odot}$), are exclusively found in the final stages of mergers (Sanders & Mirabel 1996). Significant star formation enhancements are also detected in interacting galaxies in earlier merger stages, such as those in optically selected pairs (Kennicutt et al. 1987; Xu & Sulentic 1991; Barton et al. 2000; Nikolic et al. 2004; Ellison et al. 2010; Scudder et al. 2012). Statistical studies based on large surveys have found that, among early-stage mergers, star-forming galaxies (SFGs) in close major-merger pairs (separation $\lesssim 30$ kpc and mass ratio $\lesssim 3$) have the highest star formation rate (SFR) enhancement (Xu & Sulentic 1991; Scudder et al. 2012; Patton et al. 2013). However, Spitzer observations of a sample of K_s -band-selected close major-merger pairs (Xu et al. 2010) found that only $\sim 25\%$ of the SFGs in the sample show strong enhancement in the specific star formation rate (sSFR = SFR/ M_{star}). Furthermore, the far-infrared (FIR) observations by Spitzer and

Herschel show that only SFGs in spiral+spiral (hereafter, S+S) pairs have significantly enhanced sSFR, but not those in spiral+elliptical (hereafter, S+E) pairs (Xu et al. 2010; Cao et al. 2016; Domingue et al. 2016). The Green Bank Telescope (GBT) HI observations of Zuo et al. (2018) and the IRAM CO observations of Lisenfeld et al. (2019) for paired galaxies, selected from the H-KPAIR sample of 88 close major-merger pairs that have Herschel FIR observations (Cao et al. 2016), found no significant difference between the total gas abundances of SFGs in S+E and in S+S pairs. These results reject the hypothesis that the lack of star formation enhancement in S+E pairs is due to the stripping of the cold gas of the spiral component by the ram pressure of the hot-gas halo surrounding the elliptical component (Park & Choi 2009; Hwang et al. 2011).

Simulations of interacting galaxies have shown that a massive bulge can stabilize the disk and suppress the SFR during and after close encounters (Mihos & Hernquist 1996; Cox et al. 2008; Di Matteo et al. 2008). This mechanism may play an important role in the low frequency of star formation enhancement in paired galaxies, particularly those in S+E pairs. However, there has been no observational test of the theoretical prediction in the literature. Indeed, such a test requires accurate estimates of the bulge-to-total (B/T) ratios of paired galaxies. Many works have been carried out on the task of decomposing large samples of galaxies with image fits (such as those by Simard et al. 2011; Lackner & Gunn 2012;

Meert et al. 2015; Kim et al. 2016; Meert et al. 2016). Simard et al. (2011) presented two-dimensional, point-spread function (PSF)-convolved, bulge-disk decompositions in the g and r bands on a sample of 1.1 million Sloan Digital Sky Survey (SDSS) galaxies with GIM2D (Simard et al. 2002). Lackner & Gunn (2012) worked on low-redshift ($z < 0.05$) galaxies with their own pipeline. Meert et al. (2015) carried out decompositions in the r band on 670,722 SDSS spectroscopic galaxies, a subsample of Simard et al. (2011), with GALFIT (Peng et al. 2002), and extended it to the g and i bands in Meert et al. (2016). Kim et al. (2016) provided a recipe for choosing the initial guess values of the input parameters based on galaxy color. However, these works involved automated procedures on bulk samples, without individual inspection; therefore, their results on interacting and distorted galaxies may not be reliable.

In this paper, we present our own bulge-disk decompositions for galaxies in the H-KPAIR sample (Cao et al. 2016), based on GALFIT and manual intervention deblending photometry. We study the effects of the central bulge on the star formation enhancement in paired galaxies. Using the H-KPAIR sample and a well-matched control sample, we quantify these effects and examine how much the sSFR difference between S+E and S+S pairs is caused by them. The H-KPAIR sample and control sample are introduced in Sections 2 and 4, respectively. In Section 3, we describe how we measure the B/T of H-KPAIR galaxies and compare our results with those in the literature. The science analyses are presented in Section 5, followed by a discussion in Section 6 and conclusions in Section 7. Throughout this paper, we adopt the Λ cosmology, with $\Omega_m = 0.3$, $\Omega_\Lambda = 0.7$, and $H_0 = 70 \text{ km s}^{-1} \text{ Mpc}^{-1}$.

2. The Local Close Major-merger Sample (H-KPAIR)

Our pair sample is identical with the local close major-merger H-KPAIR sample (Cao et al. 2016), which is a subsample of the complete and unbiased K_s -band-selected (Two Micron All Sky Survey, or 2MASS; Jarrett et al. 2000a, 2000b; Skrutskie et al. 2006) sample KPAIR (Domingue et al. 2009). All H-KPAIR galaxies have spectroscopic redshifts in the range of $0.0067 < z < 0.1$. The pair sample requires projected separations in the range of $5 h^{-1} \text{ kpc} \leq s(p) \leq 20 h^{-1} \text{ kpc}$, radial relative velocity $\delta(V_z) < 500 \text{ km s}^{-1}$, and K_s -band magnitude differences within 1 mag (corresponding to a mass ratio no greater than 2.5). The H-KPAIR sample contains 44 S+S pairs and 44 S+E pairs, and all have Herschel imaging observations in the six bands at 70, 110, 160, 250, 350, and $500 \mu\text{m}$ (Cao et al. 2016). Furthermore, in the H-KPAIR sample, 70 pairs have GBT 21 cm HI observations (Zuo et al. 2018) and 78 spiral galaxies are observed by the IRAM 30 m telescope for CO emissions (Lisenfeld et al. 2019).

We adopt the SFR of the H-KPAIR galaxies from Cao et al. (2016), which was derived from L_{IR} (8–1000 μm ; Sanders & Mirabel 1996), using the formula of Kennicutt (1998), with an additional correction factor of $10^{-0.20}$ for the conversion from the Salpeter initial mass function (IMF) to the Kroupa IMF (Calzetti 2013), where L_{IR} is generated from spectral energy distribution fits with the dust emission model of Draine & Li (2007).

In Cao et al. (2016), the stellar mass M_{star} of the H-KPAIR galaxies was estimated from the K_s -band luminosity using a constant mass-to-light ratio M_{star}/L_K (Xu et al. 2004; Domingue et al. 2009; Xu et al. 2012). This is because for normal galaxies, both the near-infrared emission and the stellar mass are dominated by old stellar populations, and therefore the

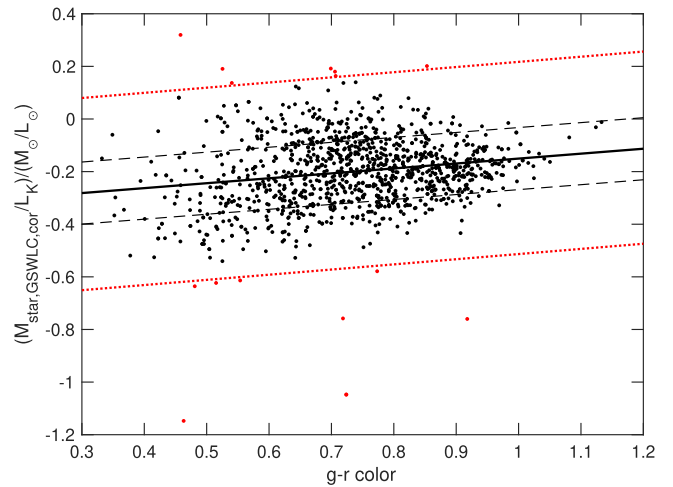


Figure 1. Correlation between the mass-to-light ratio M_{star}/L_K and the $g-r$ color. The black solid line represents the linear regression and the black dashed lines mark the 1σ deviation. The red dotted lines show the 3σ boundaries and the red dots signify the outliers excluded from the fits.

M_{star}/L_K ratio is nearly independent of galaxy type (Gavazzi et al. 1996). On the other hand, Bell & de Jong (2001) showed a color dependence of the M_{star}/L_K ratio, caused by variations of the star formation history, although this is significantly weaker than that for the mass-to-light ratio in the optical bands. In this paper, we improve the stellar mass estimate by including a $g-r$ color dependence in the M_{star}/L_K ratio. To derive the $g-r$ color for a galaxy, we create 25 mag arcsec $^{-2}$ isophotal photometry on the SDSS r -band image, using SExtractor (Bertin & Arnouts 1996), and apply the same isophotal aperture to the g -band image. For the H-KPAIR sample, we visually check and optimize the segmentations for all the pairs. When SExtractor fails to create good deblending for a merger, we manually draw polygon apertures for the galaxies, and use the 25 mag arcsec $^{-2}$ isophot of the whole merger to determine the outer boundaries of the apertures for both galaxies. We exploit the stellar mass derived in the GALEX-SDSS-WISE Legacy Catalog (GSWLC; Salim et al. 2016, 2018) for the calibration of the relation between M_{star}/L_K and $g-r$. Of 1320 of our control galaxies, 1180 have M_{star} measurements in GSWLC-2 (Salim et al. 2016, 2018). For these, we carry out a linear regression between the $M_{\text{star,GSWLC,cor}}/L_K$ and the $g-r$ color, where $M_{\text{star,GSWLC,cor}}$ is the stellar mass in GSWLC-2, after correcting the difference between the cosmology parameters used in GSWLC-2 and in this paper. After excluding the 3σ outliers iteratively, and assuming that $M_{\text{star,GSWLC,cor}}$ is a good M_{star} estimator, we obtain the following relation:

$$M_{\text{star}}/L_K = 0.19 \times (g - r) - 0.34. \quad (1)$$

The result is shown in Figure 1. The M_{star} of the galaxies in our samples are calculated using the formula in Equation (1).

3. Two-component Model Fits (GALFIT) of H-KPAIR

We carry out two-component two-dimensional fits on the SDSS r -band images with GALFIT (Peng et al. 2002). The Sérsic (1968) and Exponential (Freeman 1970) light profiles are adopted for the bulge and the disk, respectively. This method has been well tested (e.g., Meert et al. 2015; Kim et al. 2016) on the task of decomposing the bulge and the disk of SDSS local galaxies. We constrain the Sérsic index of the “bulge” component in the range of $1 \leq n \leq 8$.

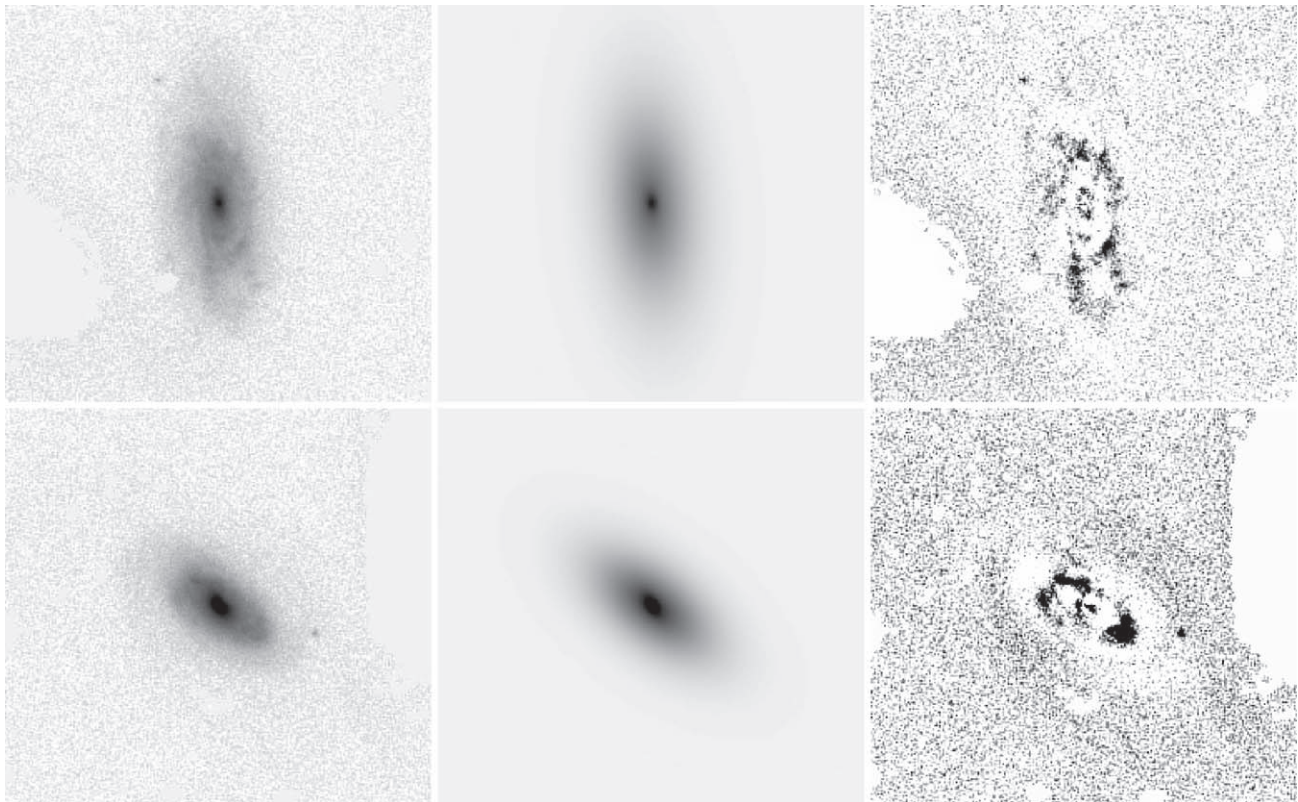


Figure 2. GALFIT results for the pair J0829+5531 (upper panels: galaxy J08291491+5531227; lower panels: galaxy J08292083+5531081; left: SDSS r -band image; middle: model image; right: residual). This is an example of satisfactory fits using the Sérsic bulge and disk models, although some substructures, such as spirals and bars, are left in the residual because of their neglect in the models.

Because some of our galaxies are on the edge of the field, or are even cut into multiple parts that are found in different fields, we use the SDSS Science Archive Server mosaic tool,⁶ which can stitch together several sky-subtracted calibrated frames⁷ to form a coherent image over a specific patch of sky, using SWarp (Bertin et al. 2002). According to Meert et al. (2015), the image should have at least 20 half-light radii to provide enough pixels for the background. We use images of 909×909 pixels uniformly for the fits of nearly all of our sample galaxies, corresponding to 0.1 of square sky, since their half-light radii constitute no more than 45 pixels, as derived from SExtractor. The only exception is galaxy J20471908+0019150 (of pair J2047+0018), the largest galaxy in our sample (size $\sim 3'$), for which an image of 1818×1818 pixels is used.

The image mask is generated based on the SExtractor segmentation image. We first run SExtractor with the detection threshold set at $25 \text{ mag arcsec}^{-2}$, to detect all the “source” from the sky background. We then identify our target galaxies visually, and set the segmentation areas of other sources for masking. We also edit the mask areas manually when SExtractor fails to deblend the sources.

The PSF is generated from the PsField files,⁸ using the code readAtlasImages-v5_4_11, provided by SDSS.⁹

We calculate an equivalent gain GAIN_{eq} and let GALFIT generate the Poisson-noise sigma image itself. GAIN_{eq} is defined as $\text{GAIN}_{\text{eq}} = \text{GAIN}/\text{cimg}$, where GAIN is the original CCD gain and cimg is the calibration factor from data numbers into nanomaggie; both are listed on the SDSS website.¹⁰

Standard GALFIT two-component fits are carried out for most H-KPAIR galaxies. Simultaneous fits of both galaxies in a pair are carried out for 61 close pairs, and the galaxies in the 16 other well-separated pairs are fitted individually. These fits yield reasonably good results, as illustrated by the examples shown in Figures 2 and 3. However, the standard GALFIT process fails to work for several extremely distorted and merging pairs, either producing large chi-squares or not converging at all. For these cases (11 merging pairs), the following special procedure is performed. First, we assume that the bulges in these systems can still be well fitted by two-dimensional models. This is because, compared to disks, bulges that are dynamically “hot” respond to tidal interactions more subtly. The triggered morphological distortions, such as the surface brightness excess in the outer regions and the slightly off-entropic inner isophotes (Kormendy 1977; Aguilar & White 1986; Davoust & Prugniel 1988; Mora et al. 2019), have a minimal effect on the two-dimensional model fits for the estimates of bulge luminosity. Accordingly, for each system, GALFIT is carried out in order to obtain the model fluxes of the bulges, while neglecting the goodness of the fits of the disks. And then, second, the total flux of each galaxy in a pair is measured by deblending photometry, using SExtractor

⁶ dr12.sdss.org/mosaics/

⁷ data.sdss.org/datamodel/files/BOSS_PHOTOOBJ/frames/RERUN/RUN/CAMCOL/frame.html

⁸ data.sdss.org/datamodel/files/PHOTO_REDUX/RERUN/RUN/objs/CAMCOL/psField.html

⁹ classic.sdss.org/dr7/products/images/read_psf.html

¹⁰ data.sdss.org/datamodel/files/BOSS_PHOTOOBJ/frames/RERUN/RUN/CAMCOL/frame.html

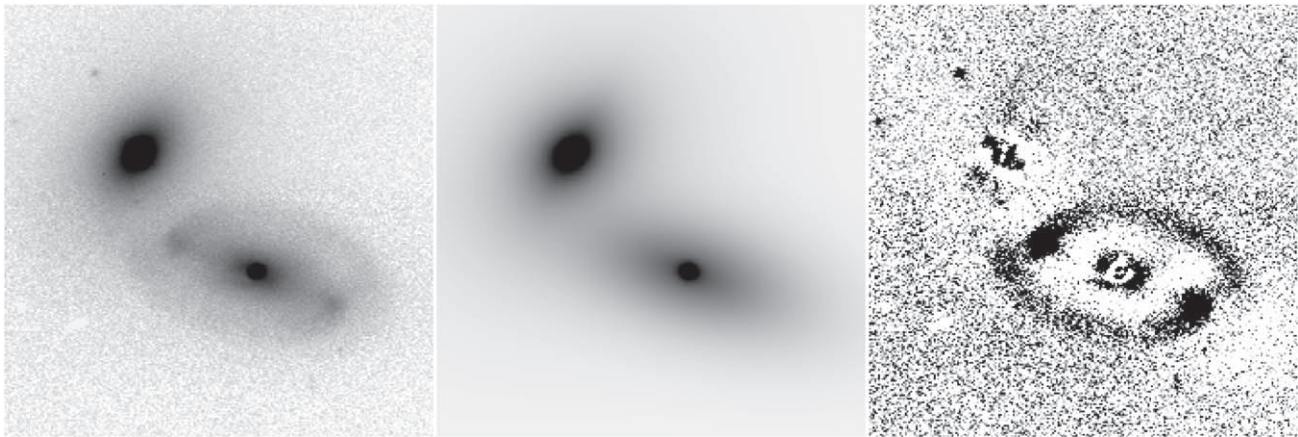


Figure 3. GALFIT results for the pair J0020+0049 (left: SDSS r -band image; middle: model image; right: residual). This is an example of simultaneous fits of both galaxies in a pair using two Sérsic bulge + disk models.

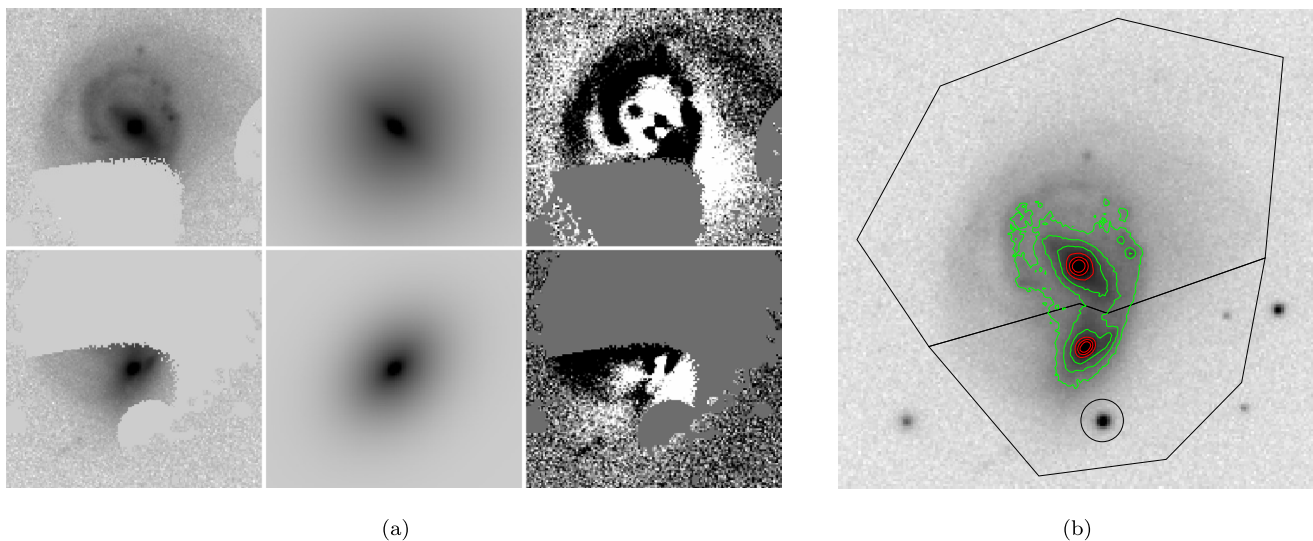


Figure 4. (a) GALFIT results of the merging pair J1444+1207 (top panels: J14442079+1207552; bottom panels: J14442055+1207429; left: SDSS r -band image; middle: model image; right: residual). (b) The polygon apertures (black) for the photometry on the total fluxes of the two galaxies and the isophotal contours of the pair. The red contour levels are at 18.5, 19, and 19.5, and the green contour levels are at 20, 20.5, and 21 mag arcsec^{-2} (no smoothing). The innermost isophot is still larger than the FWHM of the PSF. This is an example of bulge fits and deblending photometry on distorted galaxies. The compact, undistorted, high-Sérsic index component bulge is well constrained by the brightest pixels in the galaxy center, and is fitted well, although an exponential ellipse cannot reasonably represent the distorted disk.

25 mag arcsec^{-2} , or hand-drawn polygon apertures (see Section 2). An example is shown in Figure 4. The central isophotes (the red contours) of the galaxies in this example show that the bulges are not strongly distorted. Nevertheless, the B/T ratios so obtained may have larger uncertainties than those from ordinary GALFIT fits. Indeed, of the 11 merging pairs, three galaxies have a model bulge flux larger than the total flux from polygon aperture photometry. Since these are likely bulge-dominated galaxies, they are regarded as having $B/T = 1$.

The GALFIT results are listed in Table 1. Note that for the pairs where the two galaxies are fitted simultaneously, the reduced chi-square χ^2/ν is listed in the row of the first galaxy of each pair. For those where only the bulge is fitted and the total flux is obtained from the 25 mag arcsec^{-2} isophot or polygon aperture (with flag bit 2), m_{GAL} is taken from the photometry, and the disk magnitude m_{D} is calculated by subtracting the bulge flux from the total flux. Other disk

parameters of these galaxies are not available, and their χ^2/ν are not listed. We note that even though GALFIT exploits the PSF-deconvolved images, any model component with a radius significantly below the seeing (with a median FWHM of $1''.32$) shall be taken with caution.

As a quality check, in Figure 5 we compare the SExtractor 25 mag arcsec^{-2} isophotal photometry magnitude and the model magnitude (the sum of the bulges and disks) of 155 galaxies that are fitted using standard GALFIT. Because the isophotal photometry may miss fluxes from the outskirts of galaxies, especially of ellipticals, although the GALFIT models are extended to infinity, there is an offset between the isophotal and model magnitudes. For the paired galaxies in our sample, the GALFIT magnitudes m_{GAL} are on average brighter than the isophotal magnitudes by -0.11 mag, with a standard deviation of 0.17 mag. There are seven galaxies with large $m_{\text{GAL}} - m_{\text{iso}}$ deviations from the mean ($>2\sigma$), and they are flagged with Bit 4 (8, 0×1000) in Table 1. The only one with $>3\sigma$ deviation is

Table 1
GALFIT Results of H-KPAIR

ID	z	Type	m_{iso}	m_{GAL}	B/T	m_B	n_B	re	$(b/a)_B$	PA_B	m_D	rs	$(b/a)_D$	PA_D	χ^2/ν	Flag
(1)	(2)	(3)	(mag)	(mag)	(6)	(mag)	(8)	(arcs)	(10)	(deg)	(mag)	(arcs)	(14)	(deg)	(16)	(17)
J00202580+0049350	0.0149	S,J	13.66	13.72	0.11	16.12	1.58	0.9	0.71	76.6	13.85	11.5	0.45	72.7	1.12	1
J00202748+0050009	0.0162	E,J	13.39	13.01	0.97	13.05	6.78	16.3	0.77	-49.7	16.74	4.6	0.34	-30.7	...	1
J01183417-0013416	0.0453	S,J	15.60	15.63	0.37	16.72	1.00	2.2	0.50	-46.6	16.12	4.0	0.41	-80.1	1.22	1
J01183556-0013594	0.0455	S,J	14.96	14.92	0.01	19.96	8.00	0.0	0.05	-34.5	14.93	4.3	0.91	51.3	...	1
J02110638-0039191	0.0177	S,J	14.50	14.35	0.27	15.77	8.00	0.5	0.72	-28.3	14.69	6.9	0.16	-70.1	1.21	1
J02110832-0039171	0.0181	S,J	13.62	13.24	0.73	13.58	8.00	17.6	0.67	5.3	14.65	4.0	0.12	2.5	...	1
J03381222+0110088	0.0392	S,I	15.19	15.15	0.12	17.50	5.34	1.9	0.83	-36.0	15.29	5.7	0.57	45.3	1.16	1
J03381299+0109414	0.0406	E,I	15.82	15.71	0.82	15.93	5.48	2.1	0.60	51.3	17.58	2.1	0.76	3.5	1.15	1
J07543194+1648214	0.0459	S,M	14.63	14.63	0.03	18.31	1.00	0.7	0.78	28.7	14.66	2
J07543221+1648349	0.0462	S,M	14.53	14.53	0.15	16.60	1.21	2.1	0.43	-7.9	14.71	2
J08083377+3854534	0.0402	S,J	15.45	14.99	0.86	15.15	5.97	6.1	0.83	-10.1	17.12	6.5	0.42	-41.1	1.19	9
J08083563+3854522	0.0401	E,J	14.61	14.53	0.60	15.08	4.56	2.8	0.90	82.1	15.53	9.3	0.73	59.0	...	1
J08233266+2120171	0.0181	S,J	14.42	14.40	0.26	15.87	1.28	2.4	0.41	-27.5	14.72	5.0	0.73	28.5	1.21	0
J08233421+2120515	0.0181	S,J	13.80	13.71	0.39	14.74	8.00	7.3	0.33	62.6	14.25	9.2	0.42	53.7	1.22	0
J08291491+5531227	0.0251	S,J	14.09	14.02	0.03	17.75	1.00	1.7	0.42	4.1	14.05	9.8	0.44	4.4	1.15	0
J08292083+5531081	0.0252	S,J	14.04	14.07	0.11	16.50	1.77	1.4	0.38	29.4	14.19	6.1	0.52	52.0	1.16	0
J08364482+4722188	0.0526	S,J	15.18	15.29	0.19	17.07	1.60	0.9	0.39	-72.4	15.53	3.9	0.66	-58.3	1.14	1
J08364588+4722100	0.0526	S,J	14.96	14.66	0.87	14.81	5.79	6.3	0.83	-44.2	16.89	5.3	0.57	10.5	...	1
J08381759+3054534	0.0476	S,I	15.79	15.31	0.75	15.62	8.00	10.6	0.69	21.6	16.83	3.0	0.33	58.7	1.18	9
J08381795+3055011	0.0481	S,I	15.09	14.95	0.73	15.29	5.06	9.6	0.58	-32.7	16.39	4.1	0.27	-43.9	...	1
J08385973+3613164	0.0556	E,J	15.07	14.74	0.78	15.01	8.00	8.4	0.86	78.6	16.36	2.0	0.39	47.5	1.13	1
J08390125+3613042	0.0548	S,J	15.51	15.50	0.71	15.88	2.84	4.3	0.50	-56.4	16.84	3.9	0.37	-41.3	...	1
J08414959+2642578	0.0848	S,J	15.43	15.60	0.46	16.46	1.57	1.5	0.67	8.0	16.26	4.1	0.69	54.2	1.21	1
J08415054+2642475	0.0858	E,J	15.71	14.87	0.91	14.97	8.00	3.2	0.64	-47.8	17.43	2.4	0.90	26.3	...	9
J09060283+5144411	0.0291	E,J	14.48	14.41	0.59	14.99	8.00	2.4	0.25	89.8	15.38	5.2	0.34	-82.9	1.15	0
J09060498+5144071	0.0291	S,J	14.34	14.26	0.14	16.43	7.61	2.5	0.36	-87.3	14.42	6.7	0.88	62.0	1.16	0
J09123636+3547180	0.0235	E,J	109123636	13.81	0.91	13.92	5.76	7.2	0.74	52.6	16.38	30.1	0.31	-42.7	1.14	1
J09123676+3547462	0.0235	S,J	15.04	15.04	0.37	16.12	2.42	2.0	0.62	2.4	15.55	2.8	0.96	35.4	1.20	1
J09134461+4742165	0.0512	E,I	14.95	14.80	0.82	15.02	3.35	3.5	0.93	41.1	16.63	6.8	0.87	-88.5	1.21	0
J09134606+4742001	0.0527	S,I	14.89	14.80	0.43	15.71	7.52	2.5	0.46	48.1	15.41	8.0	0.43	38.4	1.24	0
J09155467+4419510	0.0396	S,M	14.97	14.62	1.00	14.62	1.00	12.2	0.56	82.2	99.00	6
J09155552+4419580	0.0396	S,M	14.14	14.14	0.20	15.91	1.00	5.3	0.39	32.6	14.38	2
J09264111+0447247	0.0891	S,M	16.21	15.94	1.00	15.94	5.61	6.0	0.82	74.9	99.00	6
J09264137+0447260	0.0907	S,M	16.17	16.17	0.70	16.56	2.93	2.4	0.46	51.7	17.46	2
J09374413+0245394	0.0242	S,I	12.85	12.85	0.09	15.44	8.00	16.8	0.24	28.4	12.96	2
J09374506+0244504	0.0235	E,I	13.47	13.29	0.82	13.50	4.77	6.2	0.63	14.1	15.16	10.8	0.88	-9.0	1.21	0
J10100079+5440198	0.0460	S,M	14.90	14.90	0.00	22.31	3.28	0.0	0.05	-0.4	14.90	2
J10100212+5440279	0.0463	S,M	15.67	15.67	0.29	17.02	2.02	1.2	0.51	42.7	16.04	2
J10155257+0657330	0.0299	S,J	15.09	15.68	0.33	16.89	1.71	1.3	0.42	-42.0	16.11	2.5	0.73	25.9	1.12	9
J10155338+0657495	0.0291	E,J	14.06	13.61	0.88	13.75	6.73	16.3	0.27	-39.2	15.94	4.4	0.78	73.3	...	1
J10205188+4831096	0.0530	S,I	16.11	15.76	0.34	16.94	3.00	0.0	0.02	60.2	16.20	3.0	0.68	-13.9	1.18	1
J10205369+4831246	0.0531	E,I	15.23	14.99	0.89	15.12	2.39	7.4	0.90	-72.0	17.41	0.4	0.40	-46.7	...	1
J10225647+3446564	0.0554	S,I	15.99	16.15	0.35	17.28	1.00	2.1	0.18	-49.2	16.63	3.1	0.52	-64.6	1.15	1
J10225655+3446468	0.0564	S,I	15.03	14.79	0.93	14.86	6.80	4.9	0.78	-60.8	17.73	3.3	0.50	-67.3	...	1
J10233658+4220477	0.0456	S,I	15.00	14.93	0.14	17.08	1.62	2.0	0.25	-84.4	15.09	4.0	0.73	-31.8	1.26	1
J10233684+4221037	0.0454	S,I	15.84	15.92	0.37	17.01	1.00	5.7	0.76	-58.2	16.42	0.9	0.68	-61.9	...	1

Table 1
(Continued)

ID	z	Type	m_{iso} (mag)	m_{GAL} (mag)	B/T	m_B (mag)	n_B	re (arcs)	$(b/a)_B$	PA_B (deg)	m_D (mag)	rs (arcs)	$(b/a)_D$	PA_D (deg)	χ^2/ν	Flag
(1)	(2)	(3)	(4)	(5)	(6)	(7)	(8)	(9)	(10)	(11)	(12)	(13)	(14)	(15)	(16)	(17)
J10272950+0114490	0.0236	S,I	14.34	14.39	0.52	15.11	1.00	4.9	0.54	-39.0	15.18	13.7	0.56	-46.0	1.21	1
J10272970+0115170	0.0234	E,I	13.56	13.35	0.70	13.74	4.49	7.7	0.70	55.8	14.64	14.6	0.65	-29.5	...	1
J10325316+5306536	0.0640	S,I	15.49	15.17	0.72	15.53	8.00	34.4	0.88	-71.3	16.54	2.6	0.26	-80.1	1.18	1
J10325321+5306477	0.0639	E,I	15.17	14.64	0.94	14.72	6.24	9.9	0.96	65.4	17.61	1.3	0.46	-50.2	...	9
J10332972+4404342	0.0523	S,J	14.79	14.75	0.26	16.19	1.59	2.2	0.21	72.6	15.08	3.4	0.72	76.1	1.22	0
J10333162+4404212	0.0521	S,J	15.65	15.62	0.13	17.80	1.00	1.9	0.24	68.1	15.78	6.8	0.14	67.1	1.20	0
J10364274+5447356	0.0458	S,I	15.34	15.34	0.79	15.59	5.57	4.2	0.82	57.1	17.04	2
J10364400+5447489	0.0458	E,I	14.34	14.34	0.88	14.48	7.34	5.6	0.80	62.6	16.60	2
J10392338+3904501	0.0435	S,J	15.26	15.20	0.38	16.26	1.88	0.9	0.74	-78.2	15.72	5.1	0.87	-49.4	1.14	1
J10392515+3904573	0.0433	E,J	14.97	14.87	0.78	15.14	4.61	3.5	0.79	12.2	16.52	7.4	0.37	-14.9	...	1
J10435053+0645466	0.0287	S,I	14.26	14.28	0.11	16.67	2.56	0.0	0.90	55.8	14.41	4.2	1.00	-43.5	1.23	1
J10435268+0645256	0.0281	S,I	14.66	14.73	0.23	16.35	1.96	2.9	0.69	11.9	15.01	7.0	0.67	16.2	...	1
J10452478+3910298	0.0268	S,J	14.44	14.45	0.46	15.28	2.83	2.8	0.74	-37.1	15.12	7.1	0.35	-10.8	1.17	1
J10452496+3909499	0.0257	E,J	13.91	13.59	0.75	13.90	8.00	13.2	0.89	14.2	15.12	13.1	0.57	69.1	...	1
J10514368+5101195	0.0250	E,J	12.94	12.72	0.66	13.17	6.04	11.7	0.69	74.5	13.90	27.5	0.49	-69.1	1.08	1
J10514450+5101303	0.0238	S,J	14.06	13.95	0.56	14.58	3.09	6.3	0.53	22.5	14.84	10.5	0.50	-9.5	...	1
J10595869+0857215	0.0632	E,J	15.02	14.67	0.81	14.90	7.05	6.9	0.95	61.3	16.50	8.1	0.55	-42.9	1.17	1
J10595915+0857357	0.0627	S,J	15.63	15.61	0.48	16.40	8.00	2.8	0.52	28.8	16.32	3.6	0.27	35.4	...	1
J11014357+5720058	0.0469	E,J	15.14	14.94	0.84	15.13	8.00	3.5	0.78	-85.7	16.94	3.1	0.58	-14.3	1.15	1
J11014364+5720336	0.0478	S,J	15.85	15.83	0.55	16.49	2.66	0.9	0.76	48.7	16.69	4.0	0.82	-20.5	...	1
J11064944+4751119	0.0643	S,I	15.48	15.35	0.87	15.50	5.88	1.7	0.78	29.1	17.58	2.2	0.35	30.8	1.20	1
J11065068+4751090	0.0654	S,I	15.23	15.29	0.87	15.44	1.00	6.7	0.45	4.7	17.51	0.5	0.63	-21.1	...	1
J11204657+0028142	0.0255	S,J	14.37	14.10	0.96	14.14	8.00	4.6	0.62	11.2	17.62	1.8	0.18	24.8	1.17	1
J11204801+0028068	0.0256	S,J	13.86	13.95	0.47	14.78	3.42	2.1	0.62	-34.7	14.63	8.7	0.15	-20.2	...	1
J11251704+0227007	0.0504	S,I	15.73	15.85	0.52	16.57	5.15	0.6	0.35	-60.7	16.64	2.6	0.42	-28.7	1.18	1
J11251716+0226488	0.0507	S,I	15.01	14.92	0.59	15.49	2.39	2.7	0.64	-79.8	15.90	7.4	0.55	32.3	...	1
J11273289+3604168	0.0351	S,J	14.36	14.28	0.54	14.95	4.59	2.8	0.49	-6.4	15.12	7.5	0.83	68.0	1.15	0
J11273467+3603470	0.0351	S,J	13.86	13.80	0.11	16.19	3.60	1.3	0.45	12.9	13.93	8.3	0.30	56.6	1.20	0
J11375476+4727588	0.0343	E,J	14.08	13.87	0.86	14.04	4.43	4.9	0.74	57.5	15.99	21.7	0.40	73.1	1.17	1
J11375801+4728143	0.0339	S,J	14.64	14.74	0.59	15.32	2.52	1.7	0.60	18.9	15.70	5.9	0.17	20.3	...	1
J11440335+3332062	0.0318	E,I	14.73	14.62	0.58	15.22	6.69	5.0	0.51	-1.3	15.56	3.4	0.50	-20.2	1.16	0
J11440433+3332339	0.0315	S,I	15.38	15.42	0.15	17.46	1.36	1.3	0.43	81.6	15.60	3.0	0.55	-14.1	1.17	0
J11484370+3547002	0.0641	S,I	16.50	16.46	0.23	18.05	1.25	3.6	0.50	75.9	16.74	6.1	0.16	82.2	1.22	1
J11484525+3547092	0.0636	S,I	14.77	14.73	0.13	16.93	2.85	2.9	0.28	-37.4	14.88	4.9	0.79	-12.8	...	1
J11501333+3746107	0.0550	S,I	15.56	15.53	0.54	16.20	2.18	1.8	0.65	-63.4	16.37	4.3	0.55	54.1	1.17	1
J11501399+3746306	0.0555	S,I	15.19	15.18	0.10	17.71	4.87	0.8	0.05	0.6	15.29	2.4	0.75	23.6	...	1
J11505764+1444200	0.0572	S,I	15.94	15.83	0.59	16.41	2.42	2.0	0.61	-83.9	16.80	8.4	0.82	-81.9	1.16	1
J11505844+1444124	0.0562	E,I	14.53	14.32	0.90	14.43	6.07	5.4	0.83	-85.3	16.84	7.6	0.55	52.0	...	1
J11542299+4932509	0.0702	S,I	15.92	15.69	0.21	17.38	8.00	0.8	0.48	-5.1	15.95	18.4	0.34	-23.9	1.14	1
J11542307+4932456	0.0712	E,I	15.35	15.12	0.59	15.70	8.00	2.3	0.55	-23.4	16.08	7.8	0.86	27.9	...	1
J12020424+5342317	0.0647	S,I	16.01	15.90	0.89	16.03	3.80	6.3	0.61	33.1	18.27	2.3	0.18	41.2	1.20	1
J12020537+5342487	0.0640	E,I	15.21	15.03	0.83	15.22	8.00	5.7	0.71	-56.6	16.97	3.9	0.77	-32.8	...	1
J12054066+0135365	0.0220	S,J	14.52	14.49	0.26	15.98	1.60	1.7	0.81	20.0	14.81	4.5	0.77	-87.5	1.15	0
J12054073+0134302	0.0209	E,J	14.05	14.01	0.51	14.75	2.22	3.2	0.71	-76.8	14.77	10.2	0.22	-83.5	1.16	0
J12115507+4039182	0.0229	S,I	14.51	14.35	0.40	15.35	8.00	9.2	0.82	42.9	14.90	2.6	0.46	53.2	1.21	1
J12115648+4039184	0.0235	S,I	14.87	14.89	0.13	17.08	8.00	4.3	0.79	53.3	15.04	3.0	0.49	-9.0	...	1

Table 1
(Continued)

ID	z	Type	m_{iso} (mag)	m_{GAL} (mag)	B/T	m_B (mag)	n_B	re (arcs)	$(b/a)_B$	PA_B (deg)	m_D (mag)	rs (arcs)	$(b/a)_D$	PA_D (deg)	χ^2/ν	Flag
(1)	(2)	(3)	(4)	(5)	(6)	(7)	(8)	(9)	(10)	(11)	(12)	(13)	(14)	(15)	(16)	(17)
J12191719+1200582	0.0273	E,I	14.61	14.43	0.56	15.06	5.65	2.7	0.67	82.5	15.33	7.6	0.98	35.1	1.14	1
J12191866+1201054	0.0268	S,I	15.14	15.24	0.37	16.32	1.00	3.3	0.27	48.8	15.73	5.8	0.45	84.3	...	1
J12433887+4405399	0.0418	S,J	14.84	14.84	0.15	16.88	4.02	2.0	0.27	62.6	15.03	5.1	0.71	-39.2	1.15	1
J12433936+4406046	0.0410	E,J	14.49	14.17	0.90	14.28	7.26	11.3	0.57	83.3	16.68	4.3	0.77	-62.0	...	1
J12525011+4645272	0.0613	S,J	15.47	15.53	0.10	18.05	1.00	0.4	0.88	-88.5	15.65	2.4	0.90	14.7	1.18	1
J12525212+4645294	0.0610	E,J	15.11	14.97	0.77	15.25	4.13	4.0	0.92	-12.9	16.57	5.6	0.72	60.3	...	1
J13011662+4803366	0.0303	S,I	14.55	14.55	0.50	15.31	1.00	9.6	0.66	19.6	15.29	2
J13011835+4803304	0.0298	S,I	15.16	15.16	0.22	16.78	1.00	11.5	0.50	51.4	15.43	2
J13082737+0422125	0.0255	S,J	15.61	15.59	0.03	19.35	4.82	0.0	0.30	-52.1	15.62	4.1	0.35	80.7	1.16	1
J13082964+0422045	0.0257	S,J	14.80	14.70	0.40	15.70	8.00	1.7	0.68	-26.0	15.26	5.4	0.70	69.1	...	1
J13131429+3910360	0.0716	E,I	15.37	15.33	0.36	16.43	2.08	0.9	0.87	41.2	15.81	3.4	0.96	84.1	1.14	1
J13131470+3910382	0.0716	S,I	16.36	15.90	0.43	16.82	2.78	1.0	0.47	25.7	16.50	16.0	0.93	80.7	...	9
J13151386+4424264	0.0359	S,I	14.55	14.61	0.20	16.35	3.01	1.3	0.50	-10.3	14.86	4.6	0.72	60.6	1.22	1
J13151726+4424255	0.0357	S,I	14.26	14.08	0.94	14.15	5.59	8.2	0.56	81.1	17.13	9.8	0.12	66.1	...	1
J13153076+6207447	0.0306	S,I	14.59	14.59	0.26	16.04	1.00	2.3	0.51	-75.5	14.92	2
J13153506+6207287	0.0306	S,I	14.57	14.57	0.16	16.56	1.00	0.9	0.09	-62.1	14.76	2
J13325525-0301347	0.0493	S,I	15.61	15.58	0.51	16.30	1.00	3.7	0.29	87.1	16.37	4.9	0.42	-76.7	1.19	1
J13325655-0301395	0.0483	S,I	14.81	14.76	0.05	17.95	8.00	1.4	0.11	77.4	14.82	4.0	0.89	21.2	...	1
J13462001-0325407	0.0248	S,J	13.97	13.93	0.68	14.34	3.95	7.7	0.40	7.4	15.17	6.9	0.42	-5.0	1.15	1
J13462215-0325057	0.0255	E,J	14.17	13.84	0.89	13.97	5.66	18.3	0.62	0.7	16.19	0.8	0.19	-3.5	...	1
J14003661-0254327	0.0256	S,I	14.26	14.21	0.70	14.59	4.76	8.5	0.72	-44.1	15.51	4.7	0.31	-71.2	1.21	1
J14003796-0254227	0.0269	S,I	14.76	14.55	0.49	15.33	3.76	1.9	0.58	13.0	15.28	7.1	0.60	-1.4	...	1
J14005783+4251203	0.0327	S,I	15.10	15.10	0.02	19.26	1.00	0.2	0.84	49.0	15.12	5.4	0.29	-11.3	1.20	1
J14005879+4250427	0.0335	S,I	15.25	15.25	0.62	15.78	1.00	6.2	0.97	22.7	16.29	1.7	0.34	69.2	...	1
J14055079+6542598	0.0306	S,J	15.49	15.50	0.29	16.85	1.36	1.6	0.66	61.9	15.87	5.3	0.28	53.3	1.16	0
J14055334+6542277	0.0308	E,J	14.55	14.17	0.89	14.30	7.58	11.6	0.67	-58.3	16.57	2.3	0.67	78.5	1.09	0
J14062157+5043303	0.0065	S,J	12.00	11.96	0.05	15.20	1.09	1.5	0.80	78.9	12.02	15.6	0.74	9.7	1.85	0
J14064127+5043239	0.0073	E,J	12.12	11.98	0.58	12.57	8.00	12.8	0.90	85.5	12.93	17.1	0.65	-68.8	1.11	0
J14070703-0234513	0.0586	S,I	15.55	15.70	0.13	17.90	3.40	0.0	0.19	-81.4	15.85	4.4	0.30	81.7	1.15	1
J14070720-0234402	0.0576	E,I	16.02	15.60	0.75	15.91	8.00	2.4	0.78	36.2	17.09	11.0	0.37	24.4	...	1
J14234238+3400324	0.0136	S,J	13.55	13.53	0.28	14.93	1.42	4.1	0.53	-80.2	13.88	7.5	0.87	3.7	1.40	0
J14234632+3401012	0.0126	S,J	13.91	13.87	0.17	15.80	1.74	2.7	0.60	10.8	14.07	8.1	0.30	35.9	1.28	0
J14245831-0303597	0.0525	S,J	15.02	15.03	0.05	18.32	3.25	0.1	0.08	51.0	15.09	2.6	0.77	41.2	1.18	1
J14245913-0304012	0.0535	S,J	15.00	14.90	0.18	16.75	2.05	1.7	0.34	33.8	15.12	10.9	0.20	37.0	...	1
J14250552+0313590	0.0371	E,I	14.53	14.22	1.00	14.22	6.55	17.9	0.78	78.3	99.00	6
J14250739+0313560	0.0375	S,I	15.64	15.64	0.55	16.29	5.90	0.9	0.74	-4.7	16.50	2
J14294766+3534275	0.0290	S,J	13.75	13.70	0.56	14.32	6.00	5.4	0.55	74.4	14.59	7.0	0.19	67.8	1.20	0
J14295031+3534122	0.0296	S,J	14.62	14.66	0.14	16.81	1.02	2.3	0.56	-61.6	14.82	5.0	0.42	12.7	1.22	0
J14334683+4004512	0.0260	S,I	13.48	13.30	0.44	14.20	8.00	32.6	0.64	-31.7	13.93	8.7	0.46	-64.0	1.24	1
J14334840+4005392	0.0264	S,I	13.91	13.79	0.80	14.04	4.01	4.6	0.68	27.2	15.54	12.3	0.78	88.5	...	1
J14442055+1207429	0.0304	S,M	14.44	14.44	0.42	15.38	6.00	5.4	0.57	-47.0	15.03	2
J14442079+1207552	0.0314	S,M	13.59	13.59	0.28	14.96	6.08	7.0	0.75	-29.9	13.95	2
J15002374+4316559	0.0311	E,J	14.08	13.76	0.69	14.16	5.04	6.1	0.91	88.4	15.03	16.3	0.73	-7.0	1.17	1
J15002500+4317131	0.0316	S,J	14.57	14.77	0.40	15.75	2.02	1.5	0.80	-29.5	15.33	3.1	0.63	-60.9	...	1
J15053137+3427534	0.0745	S,I	15.80	15.69	0.84	15.88	8.00	2.0	0.44	-89.8	17.67	4.0	0.22	-87.5	1.17	1
J15053183+3427526	0.0735	E,I	15.44	15.21	1.00	15.21	6.16	4.6	0.61	-50.9	28.88	0.5	0.05	-62.5	...	1

Table 1
(Continued)

ID	z	Type	m_{iso} (mag)	m_{GAL} (mag)	B/T	m_B (mag)	n_B	re (arcs)	$(b/a)_B$	PA_B (deg)	m_D (mag)	rs (arcs)	$(b/a)_D$	PA_D (deg)	χ^2/ν	Flag
(1)	(2)	(3)	(4)	(5)	(6)	(7)	(8)	(9)	(10)	(11)	(12)	(13)	(14)	(15)	(16)	(17)
J15064391+0346364	0.0363	S,J	14.28	14.20	0.54	14.87	8.00	1.9	0.34	81.6	15.04	6.0	0.50	71.6	1.19	0
J15064579+0346214	0.0352	S,J	14.68	14.60	0.46	15.44	4.20	4.4	0.34	-79.6	15.27	12.7	0.16	-86.8	1.19	0
J15101587+5810425	0.0303	S,J	14.63	14.46	0.35	15.59	2.29	1.2	0.72	-36.7	14.93	4.7	0.91	73.2	1.20	0
J15101776+5810375	0.0317	S,J	15.65	15.56	0.71	15.93	1.64	8.7	0.27	-28.4	16.89	2.6	0.21	-35.4	1.21	0
J15144544+0403587	0.0386	S,I	15.04	15.03	0.52	15.73	4.43	2.2	0.74	12.5	15.84	3.9	0.15	7.0	1.19	1
J15144697+0403576	0.0392	S,I	14.82	14.73	0.48	15.52	2.96	1.9	0.75	76.4	15.45	8.6	0.42	-84.1	...	1
J15233768+3749030	0.0234	S,I	15.04	15.12	0.16	17.08	1.00	4.4	0.22	65.7	15.32	3.7	0.54	-75.8	1.16	1
J15233899+3748254	0.0236	E,I	14.86	14.66	0.74	15.00	2.96	12.3	0.57	-31.2	16.11	2.0	0.78	-24.1	...	1
J15264774+5915464	0.0447	S,I	15.07	14.86	0.81	15.09	8.00	5.2	0.62	-68.3	16.64	7.9	0.24	73.9	1.14	1
J15264892+5915478	0.0455	E,I	14.96	14.90	0.85	15.08	8.00	4.8	0.58	-80.7	16.95	3.8	0.93	14.9	...	1
J15281276+4255474	0.0188	S,I	13.12	13.20	0.31	14.47	1.00	9.1	0.19	-0.6	13.61	8.3	0.45	5.1	1.45	1
J15281667+4256384	0.0180	S,I	13.40	13.19	0.77	13.47	8.00	12.6	0.56	33.3	14.80	4.0	0.19	26.9	...	1
J15523258+4620180	0.0594	E,I	15.10	14.85	0.76	15.15	7.31	5.3	0.71	1.2	16.38	5.9	0.84	-59.7	1.18	1
J15523393+4620237	0.0610	S,I	15.60	15.64	0.27	17.08	8.00	4.9	0.44	65.4	15.97	3.5	0.40	80.5	...	1
J15562191+4757172	0.0191	S,J	14.71	14.65	0.04	18.26	1.00	0.4	0.31	-70.8	14.69	7.0	0.45	-70.2	1.18	0
J15562738+4757302	0.0199	E,J	14.87	14.73	0.51	15.47	8.00	4.6	0.62	-73.6	15.51	2.3	0.75	-51.2	1.14	0
J15583749+3227379	0.0494	S,I	16.15	16.23	0.47	17.06	1.00	1.3	0.78	21.3	16.91	3.2	0.26	29.8	1.16	1
J15583784+3227471	0.0485	S,I	15.18	15.05	0.60	15.60	1.05	4.3	0.45	-17.9	16.05	8.4	0.50	-7.0	...	1
J16024254+4111499	0.0335	S,J	14.14	14.11	0.08	16.85	3.82	3.8	0.21	50.0	14.20	6.0	0.63	18.5	1.34	0
J16024475+4111589	0.0333	S,J	15.18	15.08	0.02	19.12	1.00	1.0	0.23	-7.0	15.11	4.5	0.37	68.1	1.22	0
J16080559+2529091	0.0415	S,M	15.02	15.02	0.15	17.12	1.00	0.4	0.62	-86.3	15.19	2
J16080648+2529066	0.0423	S,M	14.71	14.71	0.39	15.73	1.00	5.3	0.74	-45.5	15.24	2
J16082261+2328459	0.0409	S,J	15.00	14.88	0.04	18.45	8.00	2.4	0.23	-42.4	14.93	7.4	0.78	84.7	1.19	1
J16082354+2328240	0.0408	S,J	15.50	15.52	0.25	17.03	6.36	2.9	0.46	-54.2	15.83	2.6	0.68	54.5	...	1
J16145418+3711064	0.0582	S,I	14.64	14.62	0.74	14.94	5.08	5.6	0.73	-62.4	16.10	0.0	0.21	-57.6	1.24	1
J16145421+3711136	0.0582	E,I	15.18	14.87	0.46	15.73	3.76	2.2	0.87	15.0	15.53	7.4	0.99	-75.0	...	1
J16282497+4110064	0.0330	S,J	14.01	13.85	0.41	14.82	2.91	6.6	0.48	56.8	14.43	10.1	0.96	-9.3	1.16	1
J16282756+4109395	0.0318	S,J	14.19	14.02	0.55	14.67	8.00	16.6	0.82	-57.8	14.89	3.2	0.65	-88.1	...	1
J16354293+2630494	0.0701	S,I	15.22	14.91	0.66	15.35	8.00	10.5	0.72	33.5	16.09	4.8	0.46	-41.5	1.18	1
J16354366+2630505	0.0713	E,I	15.57	15.44	0.49	16.22	2.62	1.4	0.68	-1.6	16.16	9.1	0.51	-89.8	...	1
J16372583+4650161	0.0578	S,J	14.99	14.68	0.49	15.46	8.00	14.5	0.98	-21.2	15.42	4.7	0.31	0.1	1.16	1
J16372754+4650054	0.0568	S,J	15.14	15.16	0.02	19.17	1.00	0.6	0.75	-12.3	15.18	7.8	0.30	-1.3	...	1
J17020320+1900006	0.0573	E,I	15.09	14.79	0.38	15.83	4.37	1.7	0.84	42.7	15.32	10.7	0.66	-53.6	1.15	1
J17020378+1859495	0.0558	S,I	16.55	16.69	0.36	17.81	8.00	1.4	0.41	-37.4	17.17	4.5	0.73	64.4	...	1
J17045089+3448530	0.0572	S,I	15.99	15.56	0.48	16.34	4.39	2.6	0.56	-42.1	16.27	8.6	0.45	30.1	1.16	1
J17045097+3449020	0.0563	S,I	15.26	15.45	0.28	16.85	1.00	0.5	0.81	58.0	15.81	2.2	0.88	-87.2	...	1
J20471908+0019150	0.0130	S,J	11.85	11.47	0.34	12.66	3.31	8.4	0.82	40.9	11.92	38.5	0.64	70.2	1.28	1
J20472428+0018030	0.0116	E,J	12.16	12.46	0.68	12.89	4.82	12.4	0.75	-15.1	13.68	10.9	0.60	-13.8	...	9

Note. The columns are: (1) galaxy name; (2) redshift (after the correction for Virgocentric flow); (3) galaxy morphology: “S” for spiral and “E” for elliptical; and interaction type (Cao et al. 2016): “J” for JUS, “I” for INT, and “M” for MER; (4) magnitude, taken from the SExtractor 25 mag arcsec⁻² isophot or polygon aperture; (5) model magnitude, taken from GALFIT, except for distorted galaxies (with flag bit 2), for which this is exactly the same as the observed magnitude; (6) bulge-to-total ratio (B/T); (7) bulge magnitude; (8) bulge Sérsic index; (9) bulge effective radius, noting that all radii (re or rs) less than 0.05 are recorded as 0.0 in this table, due to the limit of the decimal places; (10) bulge axis ratio; (11) bulge position angle (the counterclockwise angle between the major axis of the ellipse and north, and the same for the disk position angle); (12) disk magnitude; (13) disk scale length; (14) disk axis ratio; (15) disk position angle; (16) reduced chi-square; and (17) binary flag in decimal number: Bit 0 (0, 0 × 0)—galaxy fitted separately; Bit 1 (1, 0 × 1)—galaxy fitted in a pair; Bit 2 (2, 0 × 10)—distorted galaxy with the bulge fitted by the model and the total flux measured by photometry; Bit 3 (4, 0 × 100)—the fitted bulge is brighter than the total flux of the galaxy obtained in aperture photometry; and Bit 4 (8, 0 × 1000)—the magnitude difference between the model and isophot is significant.

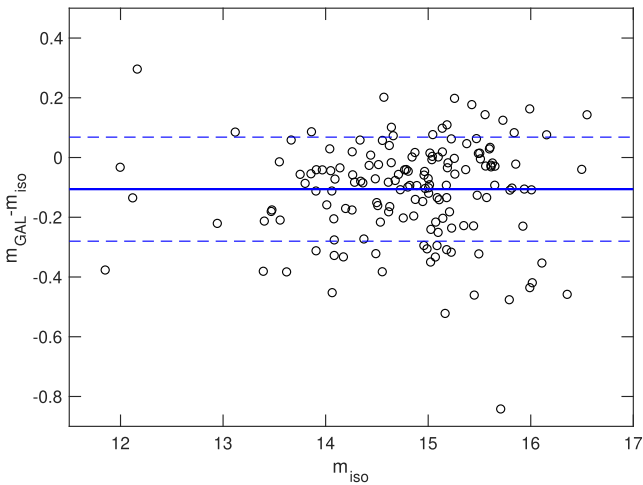


Figure 5. Magnitude differences between the GALFIT model and the SExtractor 25 mag arcsec⁻² isophotal photometry for paired galaxies. The solid line represents the mean of the differences. The dashed lines show 1 σ of the scatters.

contaminated by a nearby galaxy. We note that the GALFIT results of these galaxies should be taken with caution.

Bulges can be separated into pseudobulges and classical bulges. The pseudobulges have a Sérsic index $n = 1-2$ (Kormendy & Kennicutt 2004). Although the classical bulges may stabilize the gas disk and suppress the star formation in paired galaxies (Mihos & Hernquist 1996) and in normal galaxies (Martig et al. 2009), the pseudobulges are commonly associated with bars and nuclear disks or rings (Kormendy & Kennicutt 2004), which are disk phenomena, and which themselves may be triggered by interaction and associated with enhanced nuclear star formation (Chown et al. 2018; Erwin et al. 2021). Therefore, we treat all galaxies in our pair sample with bulge Sérsic index $n \leq 2$ as disk-only and assign $B/T = 0$ to them hereafter. It is worth noting that some pseudobulges are not related to nuclear star formation and are mostly found in late-type spirals with relatively low B/T ratios (Kim et al. 2016). Treating them as disk galaxies (i.e., $B/T = 0$) shall not introduce significant bias into our results.

For the sSFR enhancement analysis, we are only interested in the B/T ratios of spiral galaxies. Figure 6 presents separate histograms of the B/T ratio distributions of spiral galaxies in S+S and S+E pairs. We find that spiral galaxies in S+E pairs have larger bulges (at a mean $B/T = 0.35 \pm 0.05$) than their counterparts in S+S pairs (at a mean $B/T = 0.26 \pm 0.03$) statistically. In particular, 50% (44/88) of the spirals in S+S pairs are disk galaxies, with $B/T < 0.1$, while the number in S+E pairs is 32% (14/44). On the other hand, 34% (15/44) of the spirals in S+E pairs are bulge-dominated, with $B/T > 0.5$, while the percentage for those in S+S pairs is 24% (21/88).

4. Control Sample

In order to quantify the sSFR enhancement, a control sample of single spiral galaxies is selected from the catalog of Meert et al. (2015). For each paired spiral galaxy, 10 control galaxies are selected. Every control galaxy must meet the following criteria:

1. Should be identified as a spiral in Galaxy Zoo (Lintott et al. 2008).

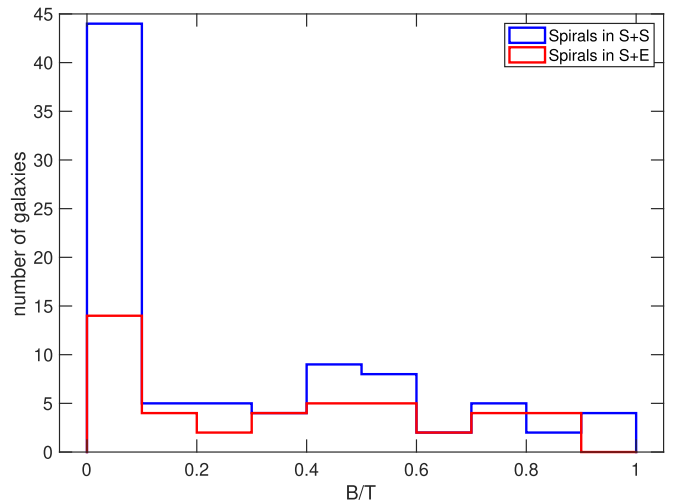


Figure 6. Histogram of the B/T ratios of the spiral galaxies in two kinds of pairs.

2. Is not in any interacting system, namely no neighboring galaxy in the SDSS database that has a projected distance ≤ 100 kpc and an observed redshift difference ≤ 1000 km s⁻¹.
3. Has a reliable B/T ratio, namely having $\chi^2/\nu < 2$ and no bad flag (flag bit 20 = 0) in Meert et al. (2015).
4. The L_K matches that of the paired galaxy within 0.1 dex (or 0.2 dex for controls of five H-KPAIR galaxies that have too few control candidates).
5. The B/T ratio matches that of the paired galaxy, with $\delta(B/T) < 0.1$, except for paired galaxies of $B/T \geq 0.8$ whose controls shall also have $B/T \geq 0.8$.
6. Match of the local density: we adopt a local density indicator $N_{1\text{Mpc}}$, which is the count of the galaxies brighter than $M_r = -19.5$ and with redshifts differing by less than 1000 km s⁻¹ from that of the target galaxy, in the surrounding sky area of radius = 1 Mpc (the count includes the target galaxy itself, if it is brighter than $M_r = -19.5$). By means of $N_{1\text{Mpc}}$, we classify galaxies into four environmental categories: field ($N_{1\text{Mpc}} \leq 3$), small group ($4 \leq N_{1\text{Mpc}} \leq 6$), large group ($7 \leq N_{1\text{Mpc}} \leq 10$), and cluster ($N_{1\text{Mpc}} > 10$). The control galaxy shall be in the same environmental category as the paired galaxy.
7. It has the closest redshift, among all the qualified candidates, to that of the paired galaxy.

Finally, we have a control sample of 1320 (1167 unique) galaxies, which are 10-to-1 matched to the 132 paired spiral galaxies in H-KPAIR. We allow galaxies to be included more than once in the control sample, as long as there is no duplication among the matches to any given paired galaxy. The M_{star} of the control galaxies are estimated from the L_K and $g-r$ color, using the same method as that for paired galaxies (see Section 2).

In order to check whether the B/T ratios obtained using our method and those estimated by Meert et al. (2015) are consistent with each other, we make the following comparison. For each paired galaxy, we pick from the 10 matching control galaxies the one with the smallest χ^2/ν in the table of Meert et al. (2015), and derive its B/T ratio using the same method that we used for the H-KPAIR galaxies. In Figure 7, our results for the B/T ratios of the 132 such galaxies in the control sample are compared with the corresponding values in Meert et al. (2015). A good overall

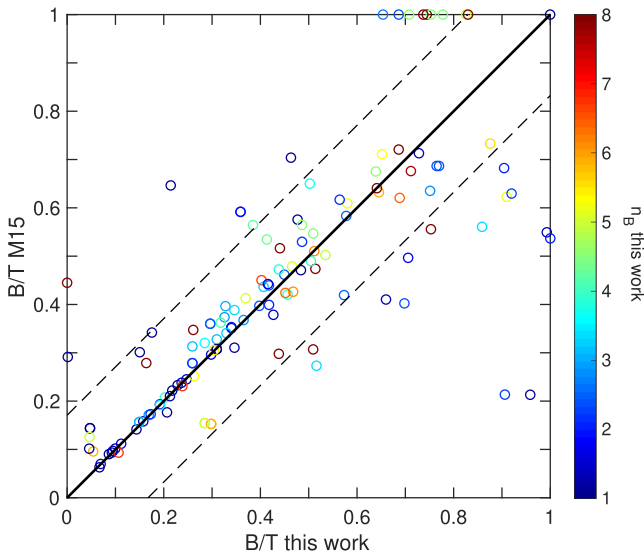


Figure 7. The B/T ratios estimated in this work compared with those of Meert et al. (2015), for a subsample of control galaxies (see the text). The solid line shows where the two results are identical to each other, and the dashed lines mark the 1σ deviations. The color bar shows the Sérsic index of the bulge component in the results of this work.

agreement is found. The average difference between the two results is only 0.002, with a standard deviation of 0.169.

It is worth noting that, as for the paired galaxies, we assign $B/T = 0$ to all control galaxies with a bulge Sérsic index $n \leq 2$. However, there is a minor difference between the paired and the control samples in this treatment: for paired samples, our GALFIT results give the n values in real numbers, while for the control sample, whose GALFIT results are taken from Meert et al. (2015), the n values are reduced to integers. This means that some of the control galaxies with $n = 2$ originally had a bulge Sérsic index in the range of $2 \leq n < 2.5$. In order to constrain the uncertainties due to this minor mismatch between the paired and the control samples, we test our results with an alternative control sample, in which galaxies with $n < 2$ (instead of $n \leq 2$) are assigned $B/T = 0$. In this case, the treatment actually applies only to control galaxies with an original bulge Sérsic index $n < 1.5$. No significant difference is found in any of our results when this alternative control sample is used.

The SFR of the control galaxies is calculated from the Wide-field Infrared Survey Explorer (WISE; Wright et al. 2010a, 2010b) W4-band $22\ \mu\text{m}$ luminosity $L_{22\ \mu\text{m}}$, using the method given by Salim et al. (2016). Namely, we estimate the total IR luminosity by fitting the luminosity-dependent IR templates of Chary & Elbaz (2001) to match the $L_{22\ \mu\text{m}}$, then use the conversion given by Kennicutt (1998), adjusted to the Chabrier IMF using the 1.58 conversion factor (Salim et al. 2007). This yields the formula

$$\log(\text{SFR}_{\text{WISE}}) = \log(L_{\text{IR,CE}}) - 9.966. \quad (2)$$

The SFR_{WISE} so defined is different from the SFRs of paired galaxies, which are estimated using Herschel data (Cao et al. 2016). In order to make the two SFRs consistent with each other, we carried out the following analysis. Of the control galaxies of Cao et al. (2016), which are matched one-to-one to H-KPAIR spirals, 82 galaxies have both Herschel and AllWISE $22\ \mu\text{m}$ SFR detections. We selected the H-KPAIR

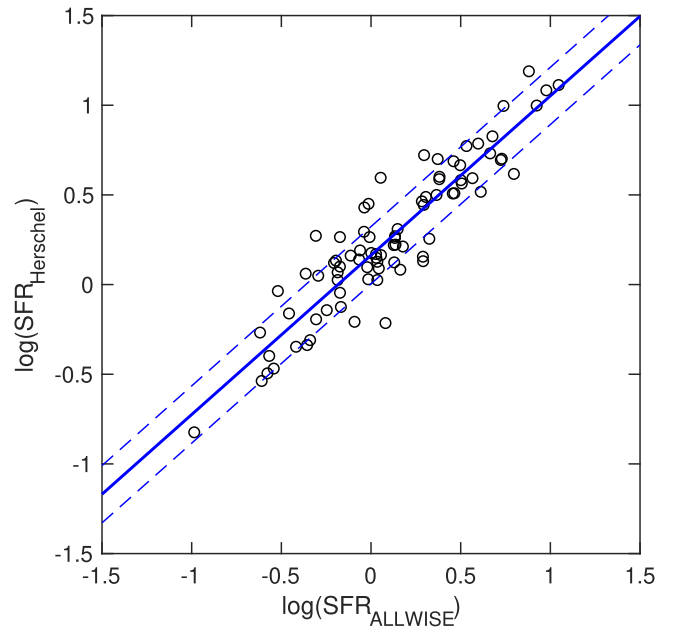


Figure 8. Comparison between $\log(\text{SFR}_{\text{Herschel}})$ and $\log(\text{SFR}_{\text{WISE}})$ for the control galaxies in Cao et al. (2016). The solid line is the linear regression, and the dashed lines represent the 1σ region.

control sample (Cao et al. 2016), instead of the pair members, to avoid any pair blending issues in the $22\ \mu\text{m}$ photometry. We carry out linear regression between the $\text{SFR}_{\text{Herschel}}$ and SFR_{WISE} of these galaxies, which is presented in Figure 8. The result shows that

$$\log(\text{SFR}_{\text{Herschel}}) = 0.89 \times \log(\text{SFR}_{\text{WISE}}) + 0.16. \quad (3)$$

This conversion is applied to the SFR_{WISE} of our control galaxies to facilitate the comparison with the paired galaxies. It is worth noting that the slightly nonlinear relation between $\text{SFR}_{\text{Herschel}}$ and SFR_{WISE} is likely due to the fact that the $22\ \mu\text{m}$ emission in the WISE W4-band is predominantly powered by massive ionizing stars ($>10 M_{\odot}$; Calzetti et al. 2007), while the total IR luminosity used in the estimate of $\text{SFR}_{\text{Herschel}}$ has significant contributions from intermediate- and low-mass stars and therefore decreases less rapidly when the massive SFR vanishes (Buat & Xu 1996). When a control galaxy has no detection in the WISE W4-band, the SFR upper limit is estimated from the upper limit of $L_{22\ \mu\text{m}}$.

5. Dependence of sSFR Enhancement on the B/T Ratio

For the individual spiral galaxies in the pair sample, we define an sSFR enhancement index sSFR_{enh} as follows:

$$\text{sSFR}_{\text{enh}} = \log(\text{sSFR}_{\text{pg}}) - \log(\text{sSFR}_{\text{med,ctrl}}), \quad (4)$$

where sSFR_{pg} is the sSFR of the paired spiral galaxy and $\text{sSFR}_{\text{med,ctrl}}$ is the median of the sSFR of the 10 control galaxies. Following Cao et al. (2016), spiral galaxies with $\log(\text{sSFR}/\text{yr}^{-1}) < -11.3$ are regarded as being in the red sequence and are thus excluded from the analysis. The remaining 98 SFGs in the H-KPAIR sample are divided into four B/T bins: disk galaxies ($B/T = 0-0.1$), galaxies with small bulges ($B/T = 0.1-0.3$), galaxies with large bulges ($B/T = 0.3-0.5$), and bulge-dominant galaxies ($B/T = 0.5-1$). Their sSFR

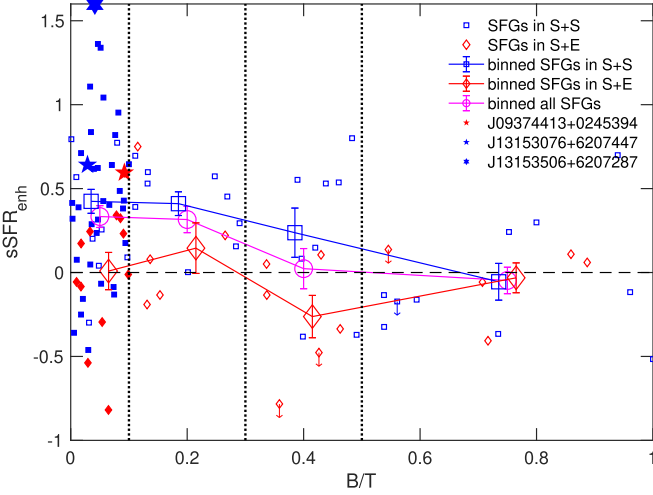


Figure 9. Plot of $s\text{SFR}_{\text{enh}}$ vs. B/T for SFGs in S+S (small blue squares) and S+E (small red diamonds) pairs. The means of the $s\text{SFR}_{\text{enh}}$ and their errors in the four B/T bins are plotted with the large symbols and error bars, with black circles for the SFGs in the total pair sample (including both S+S and S+E). The vertical dotted lines delineate the B/T bins, and the horizontal dashed line marks $s\text{SFR}_{\text{enh}} = 0$. Note that all the data points with $B/T = 0$ are plotted with a random offset toward the positive direction of the x -axis, to avoid overlap, and are shown with filled markers. Three disk galaxies with NOEMA CO observations in Xu et al. (2021) are highlighted with the pentagrams and hexagram.

enhancement is plotted against the B/T ratio in Figure 9. We use the Kaplan–Meier estimator (Kaplan & Meier 1958; Feigelson & Nelson 1985) to take into account information about the the upper limits. This shows that, for paired SFGs, on the whole, there is a significant dependence of $s\text{SFR}_{\text{enh}}$ on the B/T ratio. In particular, only the galaxies in the first two bins (with $B/T < 0.3$) have an average $s\text{SFR}_{\text{enh}}$ significantly above zero, while the average $s\text{SFR}_{\text{enh}}$ of the last two bins (with $B/T > 0.3$) are consistent with no enhancement, supporting the hypothesis that large bulges suppress interaction-induced star formation (Mihos & Hernquist 1996). Then, we divide the paired SFGs into S+S and S+E subsamples. For the SFGs in S+S pairs, the averages of $s\text{SFR}_{\text{enh}}$ in the four B/T bins show a similar but stronger trend of anticorrelation as that for the total sample. Very strong $s\text{SFR}$ enhancements ($s\text{SFR}_{\text{enh}} > 0.7$ dex) are found almost exclusively in disk SFGs ($B/T < 0.1$) in S+S pairs. On the other hand, for the SFGs in S+E pairs, the $s\text{SFR}_{\text{enh}}$ versus B/T relation is rather flat, and none of the average $s\text{SFR}_{\text{enh}}$ in the individual bins are significantly above zero. In particular, even in the first two B/T bins, with small B/T ratios, where nearly half of the SFGs in S+S pairs show strong enhancements ($s\text{SFR}_{\text{enh}} \gtrsim 0.5$), the SFGs in S+E pairs in general show no $s\text{SFR}$ enhancements.

Star formation is fueled by cold gas, and $s\text{SFR}$ can be decomposed into two terms, $s\text{SFR} = M_{\text{gas}}/M_{\text{star}} \times \text{SFE}_{\text{gas}}$, where $\text{SFE}_{\text{gas}} = \text{SFR}/M_{\text{gas}}$ is the star formation efficiency of gas. Cao et al. (2016) derived the total gas mass (M_{gas}) with a fixed gas-to-dust ratio of 100. They found significantly enhanced SFE_{gas} for SFGs in S+S pairs, but not for those in S+E pairs, compared to a control sample. On the other hand, they found no significant difference among the gas content

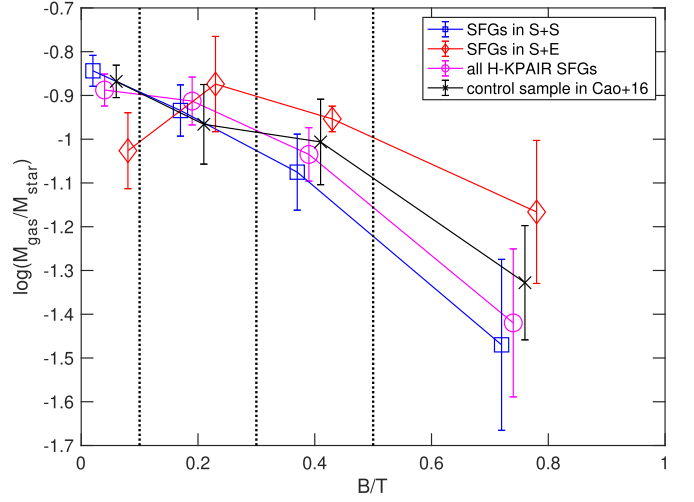


Figure 10. Plot of the means of $\log(M_{\text{gas}}/M_{\text{star}})$ and errors in four B/T bins for SFGs in S+S pairs (blue squares), S+E pairs (red diamonds), total H-KPAIR (magenta circles), and the control sample in Cao et al. (2016; black crosses).

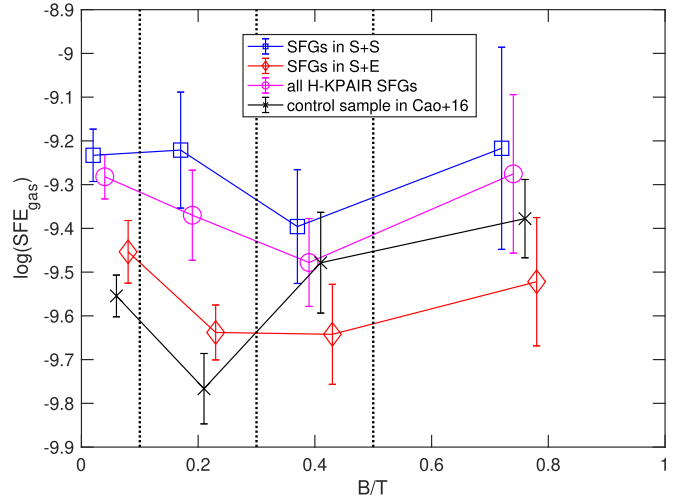


Figure 11. Plot of the means of $\log(\text{SFE}_{\text{gas}})$ and errors in four B/T bins. The meanings of the symbols are the same as in Figure 10.

($M_{\text{gas}}/M_{\text{star}}$) of SFGs in S+S pairs, in S+E pairs, and in the control sample.

In Figure 10, we show the means of $\log(M_{\text{gas}}/M_{\text{star}})$ in the four B/T ratio bins for 96 H-KPAIR SFGs with SFR detections, and for 95 SFR-detected SFGs from the control sample of Cao et al. (2016). Both the paired galaxies and the normal galaxies show a trend of the gas content decreasing with increasing B/T ratio. Consistent with Cao et al. (2016), we find no significant difference among the gas contents of SFGs in S+S pairs, in S+E pairs, and in the control sample, nor in any of the B/T bins.

In Figure 11, the means of $\log(\text{SFE}_{\text{gas}})$ in four B/T bins are plotted for the same four samples. The SFGs in S+S pairs have systematically higher SFE than those in S+E pairs, as Cao et al. (2016) showed, especially in bin 1 ($B/T < 0.1$) and bin 2 ($0.1 \leq B/T < 0.3$), where the differences are beyond 2σ . The enhanced SFE from SFGs in S+S pairs compared to that of the control samples, as found in Cao et al. (2016), also comes mainly from these two bins ($B/T < 0.3$).

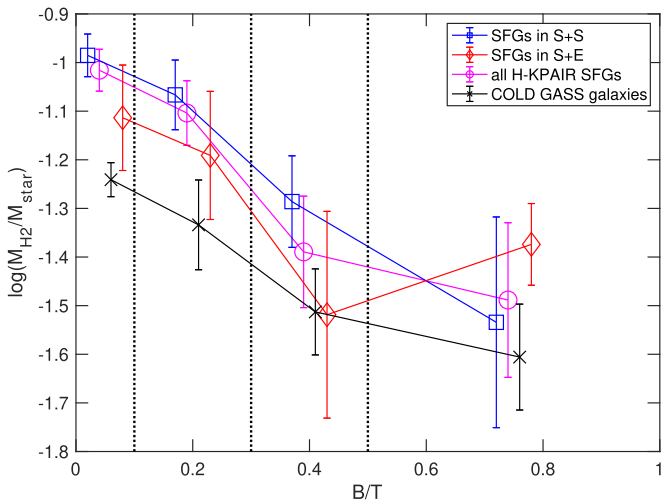


Figure 12. Plot of the means of $\log(M_{\text{H}_2} - M_{\text{star}})$ and errors in four B/T bins for SFGs in S+S pairs (blue squares), S+E pairs (red diamonds), total H-KPAIR (magenta circles), and the COLD GASS sample (black crosses).

There are two kinds of cool gas in a galaxy: atomic gas and molecular gas. The connection of SFR with molecular gas is more direct than with atomic gas. Lisenfeld et al. (2019) carried out CO observations of 78 spiral galaxies in H-KPAIR and found that, compared with normal galaxies, the paired SFGs in the H-KPAIR sample show significant enhancement in the $M_{\text{H}_2}/M_{\text{star}}$ ratio but not in SFE_{H_2} . When separated into S+S and S+E subsamples, the SFGs in S+S pairs show higher $M_{\text{H}_2}/M_{\text{star}}$ (0.21 ± 0.11 dex) and SFE_{H_2} (0.18 ± 0.06 dex) than those in S+E pairs.

In Figure 12, we plot the means of $\log(M_{\text{H}_2}/M_{\text{star}})$ in four B/T ratio bins for the 69 SFGs with WISE W4-band detections from the 78 H-KPAIR galaxies observed by Lisenfeld et al. (2019) in CO. Also plotted are the means of the $M_{\text{H}_2}/M_{\text{star}}$ ratios of 93 normal SFGs with WISE W4-band detections that have CO data in the COLD GASS sample (Saintonge et al. 2011a, 2011b) and B/T ratio data in Meert et al. (2015). The plot shows a common trend for all samples, that $M_{\text{H}_2}/M_{\text{star}}$ decreases with increasing B/T. However, the trend for paired SFGs is steeper than that for normal galaxies, and paired SFGs with small B/T ratios have significant molecular fraction enhancement, while those with $B/T > 0.5$ have about the same molecular fraction as their counterparts in the normal galaxy sample. Also, the spirals in S+E pairs show systematically lower $M_{\text{H}_2}/M_{\text{star}}$ than those in S+S pairs, as was previously found by Lisenfeld et al. (2019). The enhancement of $M_{\text{H}_2}/M_{\text{star}}$ for disk ($B/T < 0.1$) SFGs in S+S pairs is 0.26 dex ($> 4\sigma$).

In Figure 13, we show the means of $\log(\text{SFE}_{\text{H}_2})$ in four B/T bins for the same four samples. Figure 13 does not show any significant trends for any samples and, compared to the single galaxies, no significant SFE_{H_2} enhancement for the paired SFGs is found in any B/T ratio bin. Most results for the S+S and S+E subsamples have large errors because of the relatively small sample sizes. The only noticeable difference is found in the first bin of $B/T < 0.1$: the mean SFE_{H_2} of the disk SFGs in S+E pairs is 0.20 ± 0.09 dex lower than that of their counterparts in S+S pairs.

6. Discussion

Our results show that the sSFR enhancement is indeed suppressed in paired SFGs with large bulges ($B/T \geq 0.3$). In

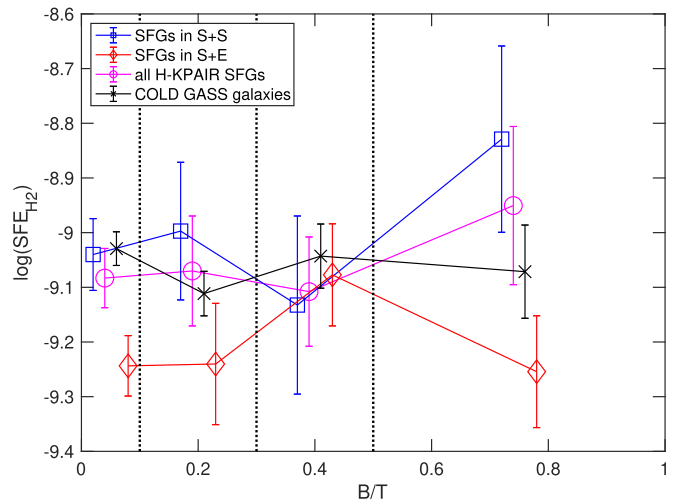


Figure 13. Plot of the means of SFE_{H_2} and errors in four B/T bins. The meanings of the symbols are the same as in Figure 12.

particular, very strong sSFR enhancement ($\text{sSFR}_{\text{enh}} \gtrsim 0.7$) occurs almost exclusively in disk galaxies with $B/T < 0.1$. However, given the large scatter of the sSFR_{enh} versus B/T relation, the low frequency of interaction-induced starbursts cannot be explained solely by the B/T dependence.

We find that spiral galaxies in S+E pairs have larger bulges than their counterparts in S+S pairs. This can partially explain the sSFR_{enh} difference between SFGs in S+E and S+S pairs found by Xu et al. (2010) and Cao et al. (2016). But it cannot explain why, in the same B/T bin, the sSFR_{enh} of SFGs in S+E pairs are systematically lower than those in S+S pairs (Figure 9). In particular, in the bin of disk galaxies ($B/T < 0.1$), SFGs in S+E pairs show significantly lower $M_{\text{H}_2}/M_{\text{star}}$ and SFE_{H_2} than their counterparts in the S+S subsample, and none of them has $\text{sSFR}_{\text{enh}} > 0.7$, while only one has $\text{sSFR}_{\text{enh}} > 0.5$.

Why do some paired disk SFGs have strong sSFR enhancements while others do not, especially those in S+E pairs? According to Xu et al. (2021), the systematically higher SFE_{H_2} of SFGs in S+S pairs than those in S+E pairs may be explained by the following scenario: the former may have a higher chance of being in low-speed coplanar interactions, which can trigger strong nuclear starbursts by tidal torques (Barnes & Hernquist 1996; Hopkins et al. 2009), while the latter are more likely to be in higher-speed, higher-incline-angle interactions, which tend to trigger ring galaxies that have more extended star formation and lower SFE_{H_2} , such as what is observed in the S+E pair Arp 142 (its spiral component has $B/T < 0.1$). This hypothesis is based on their results that, on average, S+S pairs have lower local densities and lower relative velocities than S+E pairs, therefore they are more likely to be found in a field environment that favors coplanar interactions (Dubois et al. 2014). On the other hand, S+E pairs are more likely to be found in groups/clusters where the interaction orbits are severely disturbed and randomly oriented. More investigations are needed to explore whether this mechanism can explain the difference in the sSFR_{enh} of disk SFGs in S+S and S+E pairs.

7. Conclusion

In this paper, we present a bulge–disk decomposition catalog of a 2MASS *Ks*-band-selected close major-merger galaxy pair

sample (H-KPAIR). The decompositions are derived by two-dimensional, two-component fits on SDSS r -band images, using GALFIT. With this catalog and a control sample of single galaxies selected from a large catalog of SDSS galaxies with GALFIT results (Meert et al. 2015), we are able to study the dependence of the interaction-induced sSFR enhancement on the B/T ratio, and verify the theoretical prediction that large bulges can suppress the star formation enhancement in interacting galaxies (Mihos & Hernquist 1996). We also investigate the effects of the B/T ratio dependence of the sSFR enhancement on the differences between SFGs in S+S pairs and S+E pairs. Our main results are:

1. There is a strong monotonic dependence of sSFR enhancement on the B/T ratio, in the sense that sSFR enhancement decreases with increasing B/T. On average, only paired SFGs with $B/T < 0.3$ show significant sSFR enhancement.
2. When separated into S+S and S+E subsamples, the S+S subsample shows a similar (albeit slightly stronger) trend. Very strong sSFR enhancements ($sSFR_{\text{enh}} > 0.7$ dex) are found almost exclusively in disk SFGs ($B/T < 0.1$) in S+S pairs.
3. However, for SFGs in S+E pairs, the $sSFR_{\text{enh}}$ does not show any clear B/T dependence, nor any significant enhancement in any B/T bin. The mean $sSFR_{\text{enh}}$ of SFGs in S+E pairs is lower than that of their counterparts in S+S pairs in all B/T bins.
4. Spiral galaxies in S+E pairs have higher B/T ratios than their counterparts in S+S pairs, with means of $B/T = 0.35 \pm 0.05$ and $B/T = 0.26 \pm 0.03$, respectively.
5. The total gas content ($M_{\text{gas}}/M_{\text{star}}$) and molecular gas content ($M_{\text{H}_2}/M_{\text{star}}$) are both anticorrelated with B/T for SFGs in both kinds (S+S and S+E) of pairs, and for single SFGs. Disk ($B/T < 0.1$) SFGs in S+S pairs show significant ($> 4\sigma$) $M_{\text{H}_2}/M_{\text{star}}$ enhancement. SFGs in S+E pairs have systematically lower $M_{\text{H}_2}/M_{\text{star}}$ than their counterparts in S+S pairs, and show no significant $M_{\text{H}_2}/M_{\text{star}}$ enhancement in any B/T bin. No significant difference in $M_{\text{gas}}/M_{\text{star}}$ is found between both kinds of pairs, and no $M_{\text{gas}}/M_{\text{star}}$ enhancement of paired galaxies is found in any B/T bin.
6. It appears that both the star formation efficiency as calculated by total gas ($SFE_{\text{gas}} = \text{SFR}/M_{\text{gas}}$) and by molecular gas ($SFE_{\text{H}_2} = \text{SFR}/M_{\text{H}_2}$) do not depend on the B/T ratio. There is significant SFE_{gas} enhancement for paired SFGs with $B/T < 0.3$, and the enhancement is mainly from the SFGs in S+S pairs. No significant SFE_{H_2} enhancement is found for paired SFGs in any B/T bin. The SFE_{H_2} of the disk SFGs ($B/T < 0.1$) in S+E pairs is on average 0.20 ± 0.09 dex lower than that of their counterparts in S+S pairs.

This work is supported by the National Key R&D Program of China grant No. 2017YFA0402704 and by National Natural Science Foundation of China (NSFC) grant Nos. 11873055 and 11933003, and is sponsored (in part) by the Chinese Academy of Sciences (CAS) through a grant to the CAS South America Center for Astronomy (CASSACA). C.K.X. acknowledges NSFC grant No. 11733006.

The authors would like to thank Gaoxiang Jin, Y. Sophia Dai, Cheng Cheng, Hai Xu, Piaoran Liang, Zijian Li, Dandan

Xu, Shengdong Lu, Hongming Tang, Yiru Chen, and Yilun Wang for their helpful discussions.

Funding for Sloan Digital Sky Survey IV has been provided by the Alfred P. Sloan Foundation, the U.S. Department of Energy Office of Science, and the Participating Institutions. S. D.S.S. acknowledges support and resources from the Center for High-Performance Computing at the University of Utah. The SDSS website is www.sdss.org.

SDSS is managed by the Astrophysical Research Consortium for the Participating Institutions of the SDSS Collaboration, including the Brazilian Participation Group, the Carnegie Institution for Science, Carnegie Mellon University, Center for Astrophysics | Harvard & Smithsonian (CfA), the Chilean Participation Group, the French Participation Group, Instituto de Astrofísica de Canarias, The Johns Hopkins University, Kavli Institute for the Physics and Mathematics of the Universe (IPMU) / University of Tokyo, the Korean Participation Group, Lawrence Berkeley National Laboratory, Leibniz Institut für Astrophysik Potsdam (AIP), Max-Planck-Institut für Astronomie (MPIA Heidelberg), Max-Planck-Institut für Astrophysik (MPA Garching), Max-Planck-Institut für Extraterrestrische Physik (MPE), National Astronomical Observatories of China, New Mexico State University, New York University, University of Notre Dame, Observatório Nacional / MCTI, The Ohio State University, Pennsylvania State University, Shanghai Astronomical Observatory, United Kingdom Participation Group, Universidad Nacional Autónoma de México, University of Arizona, University of Colorado Boulder, University of Oxford, University of Portsmouth, University of Utah, University of Virginia, University of Washington, University of Wisconsin, Vanderbilt University, and Yale University.

This publication makes use of data products from the Two Micron All Sky Survey, which is a joint project of the University of Massachusetts and the Infrared Processing and Analysis Center/California Institute of Technology, funded by the National Aeronautics and Space Administration and the National Science Foundation.

This publication makes use of data products from the Wide-field Infrared Survey Explorer, which is a joint project of the University of California, Los Angeles, and the Jet Propulsion Laboratory/California Institute of Technology, funded by the National Aeronautics and Space Administration.

ORCID iDs

Chuan He  <https://orcid.org/0000-0003-1761-5442>

Cong Kevin Xu  <https://orcid.org/0000-0002-1588-6700>

Donovan Domingue  <https://orcid.org/0000-0001-5662-7169>

Jia-sheng Huang  <https://orcid.org/0000-0001-6511-8745>

References

- Aguilar, L. A., & White, S. D. M. 1986, *ApJ*, 307, 97
 Barnes, J. E., & Hernquist, L. 1996, *ApJ*, 471, 115
 Barton, E. J., Geller, M. J., & Kenyon, S. J. 2000, *ApJ*, 530, 660
 Bell, E. F., & de Jong, R. S. 2001, *ApJ*, 550, 212
 Bertin, E., & Arnouts, S. 1996, *A&AS*, 117, 393
 Bertin, E., Mellier, Y., Radovich, M., et al. 2002, in ASP Conf. Ser. 281, *Astronomical Data Analysis Software and Systems XI*, ed. D. A. Bohlender, D. Durand, & T. H. Handley (San Francisco, CA: ASP), 228
 Buat, V., & Xu, C. 1996, *A&A*, 306, 61

- Calzetti, D. 2013, in *Secular Evolution of Galaxies*, ed. J. Falcón-Barroso & J. H. Knapen (Cambridge: Cambridge Univ. Press), 419
- Calzetti, D., Kennicutt, R. C., Engelbracht, C. W., et al. 2007, *ApJ*, 666, 870
- Cao, C., Xu, C. K., Domingue, D., et al. 2016, *ApJS*, 222, 16
- Chary, R., & Elbaz, D. 2001, *ApJ*, 556, 562
- Chown, R., Omori, Y., Aylor, K., et al. 2018, *ApJS*, 239, 10
- Cox, T. J., Jonsson, P., Somerville, R. S., Primack, J. R., & Dekel, A. 2008, *MNRAS*, 384, 386
- Davoust, E., & Prugniel, P. 1988, *A&A*, 201, L30
- Di Matteo, P., Bournaud, F., Martig, M., et al. 2008, *A&A*, 492, 31
- Domingue, D. L., Cao, C., Xu, C. K., et al. 2016, *ApJ*, 829, 78
- Domingue, D. L., Xu, C. K., Jarrett, T. H., & Cheng, Y. 2009, *ApJ*, 695, 1559
- Draine, B. T., & Li, A. 2007, *ApJ*, 657, 810
- Dubois, Y., Pichon, C., Welker, C., et al. 2014, *MNRAS*, 444, 1453
- Ellison, S. L., Patton, D. R., Simard, L., et al. 2010, *MNRAS*, 407, 1514
- Erwin, P., Seth, A., Debattista, V. P., et al. 2021, *MNRAS*, 502, 2446
- Feigelson, E. D., & Nelson, P. I. 1985, *ApJ*, 293, 192
- Freeman, K. C. 1970, *ApJ*, 160, 811
- Gavazzi, G., Pierini, D., & Boselli, A. 1996, *A&A*, 312, 397
- Hopkins, P. F., Cox, T. J., Younger, J. D., & Hernquist, L. 2009, *ApJ*, 691, 1168
- Hwang, H. S., Elbaz, D., Dickinson, M., et al. 2011, *A&A*, 535, A60
- Jarrett, T. H., Chester, T., Cutri, R., et al. 2000a, *AJ*, 119, 2498
- Jarrett, T. H., Chester, T., Cutri, R., et al. 2000b, 2MASS Extended Source Catalog: Overview and Algorithms, <https://doi.org/10.26131/IRSA97>
- Kaplan, E. L., & Meier, P. 1958, *J. Am. Stat. Assoc.*, 53, 457
- Kennicutt, R. C., Jr. 1998, *ApJ*, 498, 541
- Kennicutt, R. C., Jr., Keel, W. C., et al. 1987, *AJ*, 93, 1011
- Kim, K., Oh, S., Jeong, H., et al. 2016, *ApJS*, 225, 6
- Kormendy, J. 1977, *ApJ*, 218, 333
- Kormendy, J., & Kennicutt, R. C., Jr. 2004, *ARA&A*, 42, 603
- Lackner, C. N., & Gunn, J. E. 2012, *MNRAS*, 421, 2277
- Larson, R. B., & Tinsley, B. M. 1978, *ApJ*, 219, 46
- Lintott, C. J., Schawinski, K., Slosar, A., et al. 2008, *MNRAS*, 389, 1179
- Lisenfeld, U., Xu, C. K., Gao, Y., et al. 2019, *A&A*, 627, A107
- Martig, M., Bournaud, F., Teyssier, R., & Dekel, A. 2009, *ApJ*, 707, 250
- Meert, A., Vikram, V., & Bernardi, M. 2015, *MNRAS*, 446, 3943
- Meert, A., Vikram, V., & Bernardi, M. 2016, *MNRAS*, 455, 2440
- Mihos, J. C., & Hernquist, L. 1996, *ApJ*, 464, 641
- Mora, M. D., Torres-Flores, S., Firpo, V., et al. 2019, *MNRAS*, 488, 830
- Nikolic, B., Cullen, H., & Alexander, P. 2004, *MNRAS*, 355, 874
- Park, C., & Choi, Y.-Y. 2009, *ApJ*, 691, 1828
- Patton, D. R., Torrey, P., Ellison, S. L., Mendel, J. T., & Scudder, J. M. 2013, *MNRAS*, 433, L59
- Peng, C. Y., Ho, L. C., Impey, C. D., & Rix, H.-W. 2002, *AJ*, 124, 266
- Saintonge, A., Kauffmann, G., Kramer, C., et al. 2011a, *MNRAS*, 415, 32
- Saintonge, A., Kauffmann, G., Wang, J., et al. 2011b, *MNRAS*, 415, 61
- Salim, S., Boquien, M., & Lee, J. C. 2018, *ApJ*, 859, 11
- Salim, S., Rich, R. M., Charlot, S., et al. 2007, *ApJS*, 173, 267
- Salim, S., Lee, J. C., Janowiecki, S., et al. 2016, *ApJS*, 227, 2
- Sanders, D. B., & Mirabel, I. F. 1996, *ARA&A*, 34, 749
- Scudder, J. M., Ellison, S. L., Torrey, P., Patton, D. R., & Mendel, J. T. 2012, *MNRAS*, 426, 549
- Sersic, J. L. 1968, *Atlas de Galaxias Australes* (Cordoba: Observatorio Astronomico)
- Simard, L., Mendel, J. T., Patton, D. R., Ellison, S. L., & McConnachie, A. W. 2011, *ApJS*, 196, 11
- Simard, L., Willmer, C. N. A., Vogt, N. P., et al. 2002, *ApJS*, 142, 1
- Skrutskie, M. F., Cutri, R. M., Stiening, R., et al. 2006, *AJ*, 131, 1163
- Toomre, A., & Toomre, J. 1972, *ApJ*, 178, 623
- Wright, E. L., Eisenhardt, P. R. M., Mainzer, A. K., et al. 2010a, *AJ*, 140, 1868
- Wright, E. L., Eisenhardt, P. R. M., Mainzer, A. K., et al. 2010b, The Wide-field Infrared Survey Explorer (WISE): Mission Description and Initial On-orbit Performance, <https://doi.org/10.26131/IRSA1>
- Xu, C., & Sulentic, J. W. 1991, *ApJ*, 374, 407
- Xu, C. K., Lisenfeld, U., Gao, Y., & Renaud, F. 2021, *ApJ*, 918, 55
- Xu, C. K., Sun, Y. C., & He, X. T. 2004, *ApJL*, 603, L73
- Xu, C. K., Zhao, Y., Scoville, N., et al. 2012, *ApJ*, 747, 85
- Xu, C. K., Domingue, D., Cheng, Y.-W., et al. 2010, *ApJ*, 713, 330
- Zuo, P., Xu, C. K., Yun, M. S., et al. 2018, *ApJS*, 237, 2